

The evolution of the radio luminosity function of group galaxies in COSMOS

E. Vardoulaki^{1*}, G. Gozaliasl², M. Novak³, A. Finoguenov², H. G. Khosroshahi⁴

¹ Thüringer Landessternwarte, Sternwarte 5, 07778 Tautenburg, Germany

² Department of Physics, University of Helsinki, P. O. Box 64, FI-00014, Helsinki, Finland

³ Max-Planck-Institut für Astronomie, Königstuhl 17, D-69117, Heidelberg, Germany

⁴ School of Astronomy, Institute for Research in Fundamental Sciences (IPM), P.O. Box 1956836613, Tehran, Iran

Received ; accepted

ABSTRACT

To understand the role of the galaxy group environment on galaxy evolution, we present a study of radio luminosity functions (RLFs) of group galaxies based on the Karl G. Jansky Very Large Array-COSMOS 3 GHz Large Project. The radio-selected sample of 7826 COSMOS galaxies with robust optical/near-infrared counterparts, excellent photometric coverage, and the COSMOS X-ray galaxy groups ($M_{200c} > 10^{13.3} M_{\odot}$) enables us to construct the RLF of group galaxies (GGs) and their contribution to the total RLF since $z \sim 2.3$. Using the Markov chain Monte Carlo algorithm, we fit a redshift-dependent pure luminosity evolution model and a linear and power-law model to the luminosity functions. We compare it with past RLF studies from VLA-COSMOS on individual populations of radio-selected star-forming galaxies (SFGs) and galaxies hosting active galactic nuclei (AGN). These populations are classified based on the presence or absence of a radio excess concerning the star-formation rates derived from the infrared emission. We find that the fraction of radio group galaxies evolves by a factor of ~ 3 from $z \sim 2$ to the present day. The increase in the galaxy group contribution is due to the radio activity in groups being nearly constant at $z < 1$, while it is declining in the field. We show that massive galaxies inside galaxy groups remain radio active below redshift 1, contrary to the ones in the field. This evolution in the GG RLF is driven mainly by satellite galaxies in groups. Group galaxies associated with SFGs dominate the GG RLF at $z_{med} = 0.3$, while at $z_{med} = 0.8$, the peak in the RLF, coinciding with a known overdensity in COSMOS, is mainly driven by AGN. The study provides an observational probe for the accuracy of the numerical predictions of the radio emission in galaxies in a group environment.

Key words. galaxies: evolution – radio continuum: galaxies

1. Introduction

The properties and evolution of galaxies are known to be strongly linked to their external environment. Massive halos are found to play a key role in galaxy evolution. At low redshifts, it has been found that clusters of galaxies are mostly dominated by early-type galaxies composed of old stellar populations, while low-density environments host typically late-type galaxies with younger and bluer stars, producing the star-formation (SF) - density - distance to cluster centers relations and affecting the morphology of galaxies (e.g., Oemler 1974; Dressler 1980). We expect that galaxies in dense regions experience various physical processes such as tidal forces, mergers, high-speed interactions, harassment and gas stripping, which in turn contribute to dramatic morphological changes and quenching of star formations (e.g. Larson 1980; Byrd & Valtonen 1990), although, the precise timing and the relative importance of these physical processes are not yet well understood.

The environmental processes which affect galaxy evolution could, directly or indirectly influence the accretion onto the central black hole in galaxies, notably, those with a stellar bulge (Magorrian et al. 1998). Both local and large-scale processes which may affect cluster galaxies also have the potential to affect the distribution of gas in the galaxies, and hence may trigger or suppress active galactic nuclei (AGN) activity.

Apart from the role of galaxy group and cluster environment on radio emission of the brightest galaxy of the group, Khosroshahi et al. (2017) suggested that the radio luminosity of the brightest group galaxy (BGG) also depends on the group dynamics, in a way that BGGs in groups with a relaxed/virialised morphology are less radio luminous than the BGG with the same stellar mass but in an evolving group. This was supported numerically by a semi-analytic approach (Raouf et al. 2018), where they made a prediction of the radio power for the first time. However without an observational constraint reaching high redshift, the numerical models cannot be constrained.

Many radio studies (Best et al. 2002; Barr et al. 2003; Miller & Owen 2003; Reddy & Yun 2004) showed an increase in radio-loud AGN activity in galaxy clusters, at a range of redshifts and in both relaxed and merging systems. The radio emission (< 30 GHz) in galaxies is dominated by synchrotron radiation from accelerating relativistic electrons, with a fraction of free-free emission (e.g., Sadler et al. 1989; Condon 1992; Clemens et al. 2008; Tabatabaei et al. 2017). The feedback from supernovae explosions in star-forming galaxies (SFGs) and that from the growth of the central supermassive black hole (SMBH) in AGN are two main sources of acceleration of cosmic electrons.

For the purpose of using radio emission as a proxy for measuring star formation rates (SFRs) or AGN feedback, it is important to estimate which process dominates the radio emission: star formation processes, or SMBH accretion. We follow the method demonstrated in (Delvecchio et al. 2017) who measured the ra-

* email: elenivard@gmail.com

radio excess compared to the total star-formation-based infrared (IR) emission. Objects which exhibit radio excess above what is expected from star formation alone, as calculated from their infrared emission, are deemed AGN, and the rest are SFGs. These populations contribute different percentages to the energy budget. In the radio, this is quantified by calculating the radio luminosity function (RLF). Novak et al. (2018) studied the 3 GHz VLA-COSMOS RLF and calculated the relative contributions to the RLF from the AGN and SFG populations, down to submicrojansky levels, and found that the RLF can reproduce the observed radio sky brightness very well. AGN and SFGs contribute differently to the RLF, where AGN are known to dominate the bright part of the RLF, and SFGs dominate the faint. In particular, 90% of the population at the faint end ($< 0.1 \mu\text{Jy}$) is linked to SFGs. In clusters of galaxies, Yuan et al. (2016) who studied the RLF of brightest cluster galaxies (BCGs) up to $z = 0.45$ found no evolution, and a dominant population of AGN, as most of their BCGs are associated with AGN. Branchesi et al. (2006) compared clusters at $0.6 < z < 0.8$ to the local Abell clusters and found very different RLFs. These studies target populations dominated by AGN, and thus probe the high end of the radio luminosity function. The question arises, how much do smaller mass environments, those of groups of galaxies, and their members contribute to the observed radio sky brightness.

In this paper we investigate the population of galaxies inside X-ray galaxy groups in the COSMOS field (Gozaliasl et al. 2019) to quantify their contribution to the RLF at 3 GHz VLA-COSMOS (Novak et al. 2018; Smolčić et al. 2017b). In Section 2 we describe the X-ray and radio data used throughout this work. In Section 3 we focus on methods for deriving the RLF and its evolution through cosmic time. In Section 4 we present and discuss the results on the RLF of group galaxies, and calculate their contribution to the total RLF at 3 GHz. We further separate the galaxies to BGGs and satellites (SGs). We also use the radio excess parameter and the presence of jets/lobes to disentangle AGN and SFGs in the radio, and provide the relative contributions of these populations to the group galaxies (GG) RLF and to the total RLF. This is presented in Section 5. Finally, in Section 6 we provide a brief summary. The tables with the results of the analysis can be found in the Appendix.

We assume flat concordance Lambda Cold Dark Matter (Λ CDM) cosmology defined with a Hubble constant of $H_0 = 70 \text{ km s}^{-1} \text{ Mpc}^{-1}$, dark energy density of $\Omega_\Lambda = 0.7$, and matter density of $\Omega_m = 0.3$. For the radio spectral energy distribution we assume a simple power law described as $S_\nu \propto \nu^{-\alpha}$, where S_ν is the flux density at frequency ν and α is the spectral index. If not explicitly stated otherwise, $\alpha = 0.7$ is assumed.

2. The Data

The Cosmic Evolution Survey (COSMOS) is a deep multi-band survey covering a 2 deg^2 area, thus offering a comprehensive data-set to study the evolution of galaxies and galaxy systems. The full definition and survey goals can be found in Scoville et al. (2007).

The sample selection for this study is described below. We used radio selected samples of galaxies which have been cross-matched with multi-wavelength optical/near-infrared (NIR) and value-added catalogues in the COSMOS field. The radio data have been selected from the VLA-COSMOS 3 GHz Large Project (Smolčić et al. 2017b), with a median sensitivity of $2.3 \mu\text{Jy beam}^{-1}$ and resolution of 0.75 arcsec. The cross-correlation of the radio and multiwavelength sources can be found in Smolčić et al. (2017a). Only sources within the COS-

MOS2015 catalogue (Laigle et al. 2016) or with *i*-band counterparts have been given the availability of reliable redshift measurements. The COSMOS2015 catalogue contains the high-quality multiwavelength photometry of $\sim 800\,000$ sources across more than 30 bands from near-ultraviolet (NUV) to near-infrared (NIR) through a number of surveys and legacy programs (see Laigle et al. 2016, for detailed description).

On completion of the visionary Chandra program (Elvis et al. 2009; Civano et al. 2016), high-resolution imaging across the full COSMOS field became available. Furthermore, more reliable photometric data provided a robust identification of galaxy groups at a higher redshift, thus resulting in a revised catalogue of extended X-ray sources in COSMOS (Gozaliasl et al. 2019) which is obtained by combining both the Chandra and XMM-Newton data for the COSMOS field. We use this galaxy groups catalogue (Gozaliasl et al. 2019) for our analysis. Within the virial radius of these groups, the above selection criteria resulted in a total of 306 objects distributed in the galaxy groups. The brightest group galaxy (BGG) is the most massive and generally the most luminous galaxy in *r*-band within the virial radius associated with the extended X-ray emission. The rest of group galaxies (GGs) are labelled as satellites (SGs). The details of the sample selection and the accuracy of the group findings using spectroscopic and photometric redshifts can be found in Gozaliasl et al. (2019). In Fig. 1 we present the data for the group galaxies used in our analysis. The spectroscopic redshifts are available for 35% of our sources and the median accuracy of the photometric redshifts is $\Delta z / (1 + z_{\text{spec}}) = 0.01(0.04)$.

To perform our analysis on the radio luminosity function of group galaxies in COSMOS, we cross-match the galaxy group catalogue and the 3 GHz VLA-COSMOS data with radius of $0.8''$. We furthermore use the 3 GHz VLA-COSMOS data presented in Novak et al. (2018), who constructed RLFs up to $z \sim 5.5$, to compare to the total RLF in COSMOS up to $z \sim 2.3$. Furthermore, Novak et al. (2018) separated objects in SFGs and AGN, following the radio excess prescription of Delvecchio et al. (2017). This method is based on the excess radio emission from what is expected from star formation alone. Delvecchio et al. (2017) fitted the infrared spectral energy distribution of radio sources at 3 GHz VLA-COSMOS and calculated the contribution of the 3 GHz VLA-COSMOS radio sources to the radio luminosity, by applying a conservative cut. Galaxies which exhibit an excess in radio emission above 3σ from what is expected from SF alone were deemed AGN, with the rest being SFGs. This method was used to separate the Novak et al. (2018) sample which we use here for comparison, in SFGs and AGN. Finally, Novak et al. (2018) described possible biases and uncertainties associated with the data sample selection and thus we refer the reader to this reference.

3. Methods and analysis

We describe the process of calculating the RLF for galaxies in groups in COSMOS (Gozaliasl et al. 2019) using the VLA-COSMOS 3 GHz data. We applied a cut in group mass $M_{200c} > 10^{13.3} M_\odot$, to account for a difference in the limiting mass of the group catalog with redshift. We further separate group galaxies in BGGs and SGs. We compare to the RLF of the population of SFGs and AGN at 3 GHz VLA-COSMOS in the same redshift bins, and to the total RLF calculated from the 3 GHz data (Novak et al. 2017; Smolčić et al. 2017b). We fit linear and power-law models to the RLFs of GGs and compare them to the total RLF to obtain the contribution of GGs to the total RLF at 3 GHz

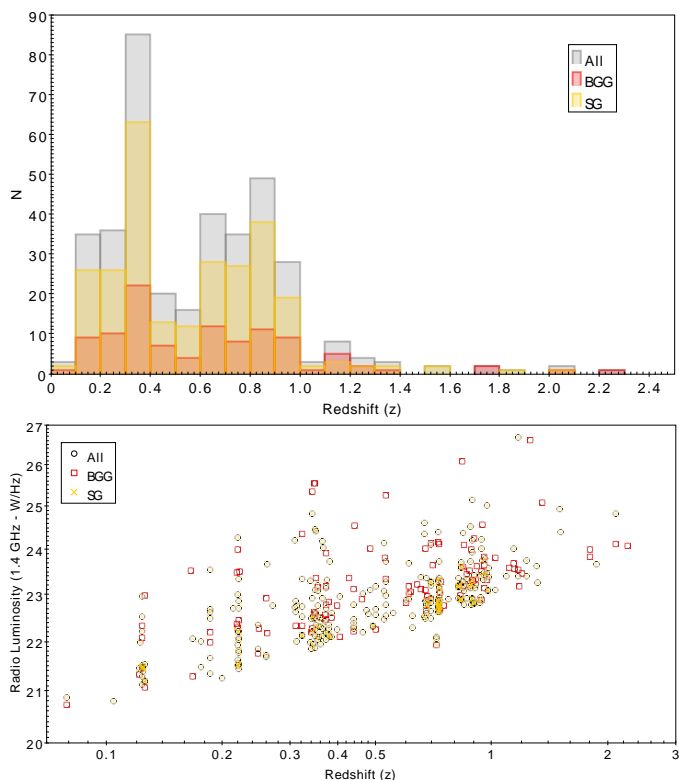


Fig. 1. Top: Number of sources per redshift. Bin size is 0.1. Bottom: Radio luminosity at 1.4 GHz versus redshift. The redshift plotted is the one of the galaxy groups. The radio luminosity is calculated from the 1.4 GHz flux density for the redshift of the object. Black represents all group galaxies, red is for BGGs, and yellow is for SGs (see Sec. 2 for clarification on the classification).

VLA-COSMOS, something that has not been shown before in COSMOS.

3.1. Measuring the radio luminosity function

To obtain the total RLFs, for GGs, SFGs and AGN, we followed the method adopted by Novak et al. (2017) (see their Sec. 3.1). They computed the maximum observable volume V_{\max} for each source (Schmidt 1968) and simultaneously applied completeness corrections that take into account the non-uniform *rms* noise and the resolution bias (see Sec. 3.1 in Novak et al. 2017). Then the RLF is

$$\Phi(L, z) = \frac{1}{\Delta \log L} \sum_{i=1}^N \frac{1}{V_{\max,i}} \quad (1)$$

where L is the rest-frame luminosity at 1.4 GHz, derived using the radio spectral index of a source calculated between 1.4 GHz (Schinnerer et al. 2010) and 3 GHz (Smolčić et al. 2017b), and $\Delta \log L$ is the width of the luminosity bin. The radio spectral index should remain unchanged between frequencies, and is only available for a quarter of the 3 GHz VLA-COSMOS sample. For the rest of the sources detected only at 3 GHz, we assumed $\alpha = 0.7$. The latter corresponds to the average spectral index of the entire 3 GHz population (see Sec. 4 in Smolčić et al. 2017b). V_{\max} is the maximum observable volume given by

$$V_{\max,i} = \sum_{z=z_{\min}}^{z_{\max}} [V(z + \Delta z) - V(z)]C(z), \quad (2)$$

where the sum starts at z_{\min} and adds co-moving spherical shells of volume $\Delta V = V(z + \Delta z) - V(z)$ in small redshift steps $\Delta z = 0.01$ until z_{\max} . $C(z)$ is the redshift-dependent geometrical and statistical correction factor. This takes into account sample incompleteness. For a thorough description of the biases see Section 6.4 in Novak et al. (2017). The correction factor is given by

$$C(z) = \frac{A_{\text{obs}}}{41253 \text{ deg}^2} \times C_{\text{radio}}(S_{3\text{GHz}}(z)) \times C_{\text{opt}(z)}, \quad (3)$$

where $A_{\text{obs}} = 1.77 \text{ deg}^2$ is the effective unflagged area observed in the optical to NIR wavelengths, C_{radio} is the completeness of the radio catalogue as a function of the flux density $S_{3\text{GHz}}$, and C_{opt} is the completeness owing to radio sources without assigned optical-NIR counterpart. Completeness corrections are shown in Smolčić et al. (2017b) in their Fig. 16 and Table 2, and in Novak et al. (2017), in their Fig. 2.

The redshift bins are large enough not to be affected severely by photometric redshift uncertainty, and follow the selection of Novak et al. (2017) to allow comparisons. Luminosity bins in each redshift bin span exactly the observed luminosity range of the data. In order to eliminate possible issues due to poorer sampling, the lowest luminosity has a range of values from the faintest observed source to the 5σ detection threshold at the upper redshift limit (corresponding to $5 \times 2.3 \mu\text{Jy beam}^{-1}$ at 3 GHz). The reported luminosity for each RLF is the median luminosity of the sources within the bin. The RLFs for all group galaxies are shown in Fig. 2 (black points) and are also listed in Table A.1. The RLFs for the BGGs and SGs are also shown in Fig. 2 (red squares/yellow stars), and are listed in Tables A.2 and A.3, respectively. The low- z bin in Fig. 4 is split in two halo mass M_{200c} bins, above and below $10^{13.3} M_{\odot}$, and for our further analysis we use the values above. We note that at $1.6 < z < 2.3$ we have only 2 SGs above our halo-mass cut ($M_{200c} > 10^{13.3} M_{\odot}$), thus we do not calculate their RLF. This is related to limits in the radio power that are probed at those redshifts, leading to low statistics as well as scarcity of massive groups. As discussed in Novak et al. (2018), there is only 5-10% loss of completeness on the optical/NIR counterparts above $z \sim 2$.

3.2. The total RLF at 3 GHz VLA-COSMOS

We use the total RLF derived from the SFG and AGN populations at 3 GHz VLA-COSMOS (Novak et al. 2017, 2018; Smolčić et al. 2017c) to compare to the RLF values derived for the group galaxies in COSMOS. The RLF of the SFG and AGN populations are calculated in the same way and for the same redshift bins as described above, and for the same area coverage as the galaxy groups in COSMOS. To fit the RLF two models are used in literature (e.g., Condon 1984; Sadler et al. 2002; Grupcioni et al. 2013), the pure luminosity evolution (PLE) and the pure density evolution (PDE). The RLF is fitted under the assumption that its shape remains unchanged at all observed cosmic times. Only the position of the turnover and normalisation can change with redshift. This corresponds to the translation of the local LF in the $\log L - \log \Phi$ plane (Condon 1984) and can be divided into pure luminosity evolution (horizontal shift) and pure density evolution (vertical shift).

To describe an RLF across cosmic time, the local RLF is evolved in luminosity, or density, or both (e.g. Condon 1984). This is parametrised (Novak et al. 2018) using two free parameters for density evolution (α_D, β_D), and two for luminosity evo-

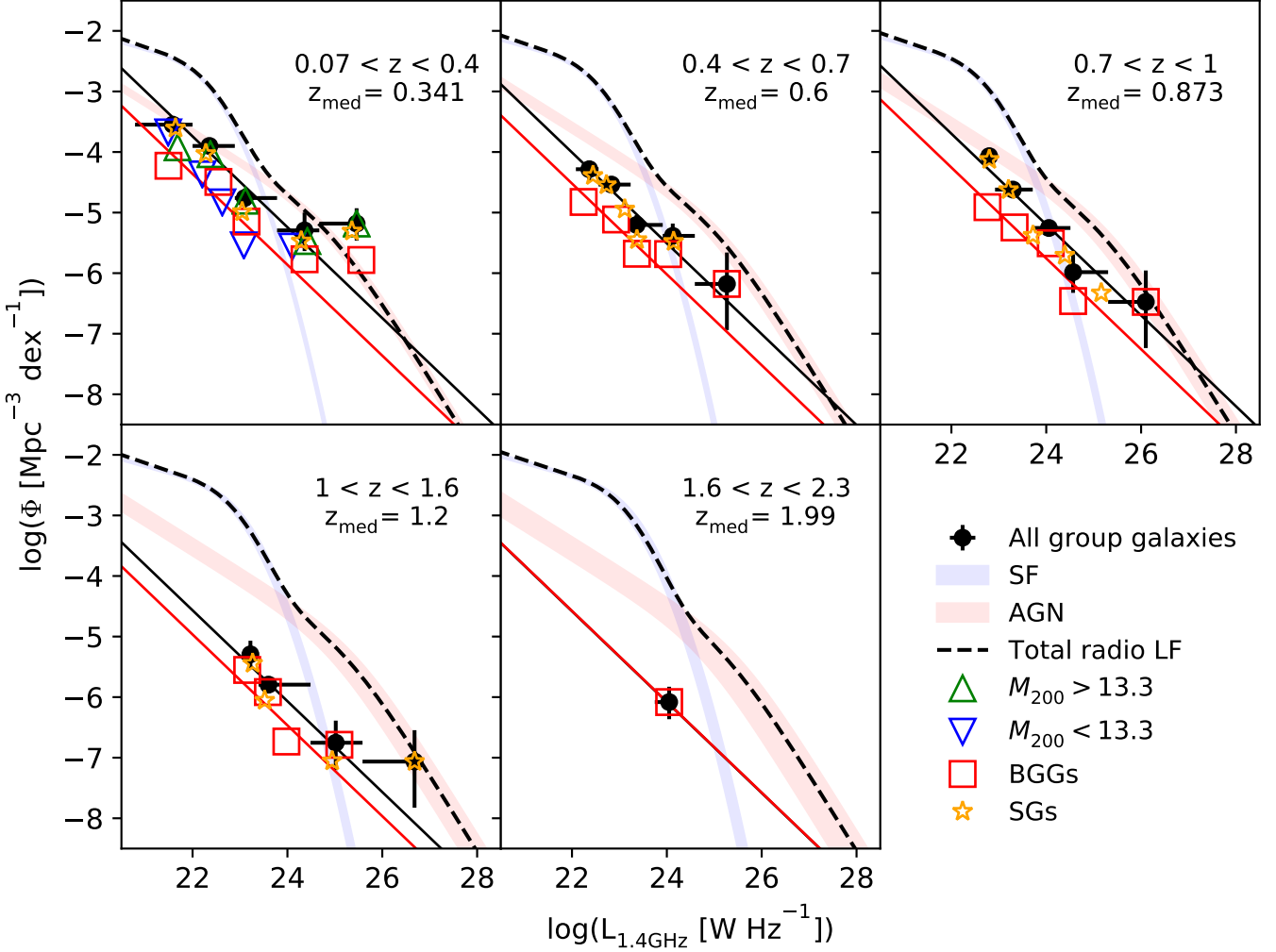


Fig. 2. Total radio luminosity functions of galaxies in groups. Black points indicate the RLFs for group galaxies derived using the V_{\max} method (see Section 3.1). Red squares and yellow stars mark brightest group galaxies and satellites, respectively. The blue and red shaded areas show the $\pm 3\sigma$ ranges of the best-fit evolution for the individual SFG and AGN populations, respectively (outlined in Section 3.2). The black dashed line is the fit to the total RLF at 3 GHz VLA-COSMOS (Novak et al. 2017; Smolčić et al. 2017c). The black solid line is the fit to the group galaxies RLF, and the red solid line is the best fit for BGGs, as explained in Section 3.3. We do not show the best fit for SGs for clarity. For the low- z sub-samples ($z < 0.4$), the halos have been split into massive ($M_{200c} > 10^{13.3} M_{\odot}$) and low-mass halos ($M_{200c} < 10^{13.3} M_{\odot}$).

lution (α_L, β_L) to obtain

$$\Phi(L, z, \alpha_L, \beta_L, \alpha_D, \beta_D) = (1+z)^{\alpha_D + z\beta_D} \times \Phi_0 \left(\frac{L}{(1+z)^{\alpha_L + z\beta_L}} \right), \quad (4)$$

where Φ_0 is the local RLF. Since the shape and evolution of the RLF depend on the galaxy population type, Novak et al. (2017) used a power-law plus log-normal shape of the local RLF for SFGs. They used the combined data from Condon et al. (2002), Best et al. (2005) and Mauch & Sadler (2007) to obtain the best fit for the local value

$$\Phi_0^{\text{SF}}(L) = \Phi_{\star} \left(\frac{L}{L_{\star}} \right)^{1-\alpha} \exp \left[-\frac{1}{2\sigma^2} \log^2 \left(1 + \frac{L}{L_{\star}} \right) \right], \quad (5)$$

where $\Phi_{\star} = 3.55 \times 10^{-3} \text{ Mpc}^{-3} \text{ dex}^{-1}$, $L_{\star} = 1.85 \times 10^{21} \text{ W Hz}^{-1}$, $\alpha = 1.22$, and $\sigma = 0.63$.

It was noted by Novak et al. (2017) that the PDE of SF galaxies would push the densities to very high numbers, thus making them inconsistent with the observed cosmic star formation rate

densities. This is a consequence of the fact that our data can constrain only the bright log-normal part of the SF RLF. For AGN it was shown by Smolčić et al. (2017c) that the PDE and PLE models are similar, mostly because the shape of the RLF does not deviate strongly from a simple power law at the observed luminosities. Considering the above reasoning while also trying to keep the parameter space degeneracy to a minimum, we decided to use only the PLE for our analysis. Thus we adopt the approach of Novak et al. (2018) who fitted the total RLF for SFG and AGN populations by constructing a four-parameter redshift-dependent pure luminosity evolution model with two parameters for the SFG and AGN populations of the form:

$$\begin{aligned} \Phi(L, z, \alpha_L^{\text{SF}}, \beta_L^{\text{SF}}, \alpha_L^{\text{AGN}}, \beta_L^{\text{AGN}}) = \\ = \Phi_0^{\text{SF}} \left(\frac{L}{(1+z)^{\alpha_L^{\text{SF}} + z\beta_L^{\text{SF}}}} \right) + \Phi_0^{\text{AGN}} \left(\frac{L}{(1+z)^{\alpha_L^{\text{AGN}} + z\beta_L^{\text{AGN}}} \right), \quad (6) \end{aligned}$$

where Φ_0^{SF} is the local RLF for SFGs as in Eq. 5, and for the non-local Universe is a function of the quantity in the parenthesis,

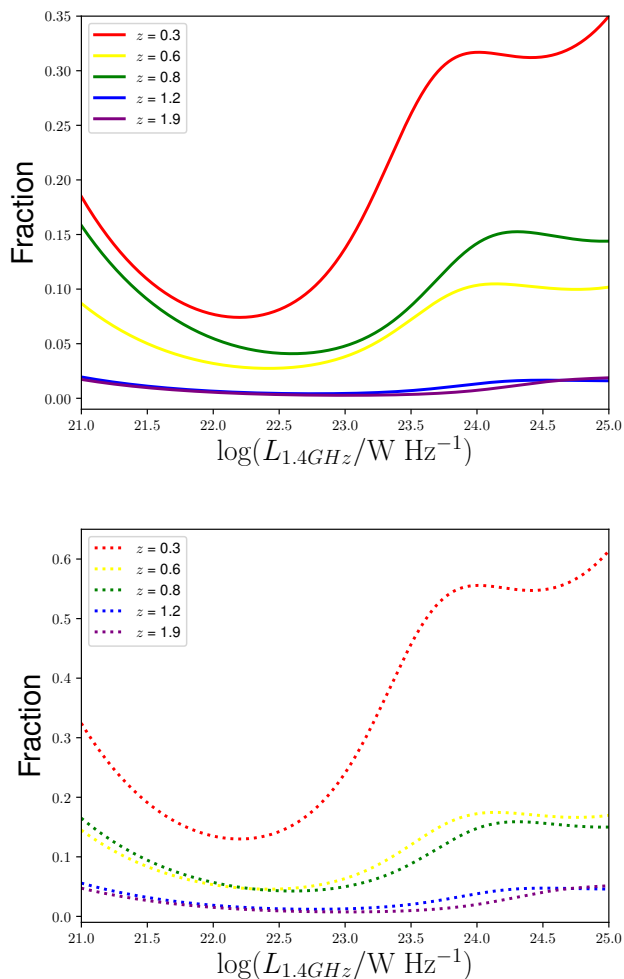


Fig. 3. Top: Fraction for group galaxies showing their contribution to the total 3 GHz radio luminosity function at different epochs vs radio luminosity at 1.4 GHz. Colours represent different redshift bins. At redshifts > 1 , both the low and the high radio emission fraction remains constant. As the universe evolves the fraction of the high radio emission increases dramatically. Bottom: Same as above, but for all massive galaxies ($M_* > 10^{11.2} M_\odot$) with radio emission at 3 GHz (Smolčić et al. 2017a; Laigle et al. 2016).

$L/(1+z)^{\alpha_L^{\text{SF}}+z\beta_L^{\text{SF}}}$. Φ_0^{AGN} is the local RLF for AGN of the form

$$\Phi_0^{\text{AGN}}(L) = \frac{\Phi_\star}{(L_\star/L)^\alpha + (L_\star/L)^\beta}, \quad (7)$$

where $\Phi_\star = \frac{1}{0.4} 10^{-5.5} \text{ Mpc}^{-3} \text{ dex}^{-1}$, $L_\star = 10^{24.59} \text{ W Hz}^{-1}$, $\alpha = -1.27$, and $\beta = -0.49$ (Smolčić et al. 2017c; Mauch & Sadler 2007), and for the non-local Universe is a function of the quantity $L/(1+z)^{\alpha_L^{\text{AGN}}+z\beta_L^{\text{AGN}}}$.

Novak et al. (2018) used the Markov chain Monte Carlo (MCMC) algorithm, available in the Python package `emcee` (Foreman-Mackey et al. 2013), to perform a multi-variate fit to the data. The redshift dependence of the total evolution parameter $\alpha + z \cdot \beta$ (see Eq. 6) is necessary to describe the observations at all redshifts. The best fit values, based on the results of Novak et al. (2018), for SFGs are $\alpha_L^{\text{SF}} = 3.16$ and $\beta_L^{\text{SF}} = -0.32$, and for AGN are $\alpha_L^{\text{AGN}} = 2.88$ and $\beta_L^{\text{AGN}} = -0.84$. The α_L and β_L values for both SFGs and AGN are valid for $z < 5.5$ and within the redshift range of our sample of group galaxies. We use these values to plot the fit to the RLF for SFGs and AGN in Fig. 2, shown

in blue and red lines, respectively. The total RLF (including all SFG and AGN), is shown as a dashed black line in Fig. 2.

3.3. Fitting the RLF of group galaxies and comparing to the total 3 GHz RLF

We fit a linear regression to the radio luminosity function of the group galaxies, and separately of the BGGs and SGs, from redshifts 0.07 to 2.3 of the form

$$y = \Phi_\star / (L_\star^\gamma) * L^\gamma, \quad (8)$$

where L_\star is arbitrarily chosen to be $10^{24} \text{ W Hz}^{-1}$, and Φ_\star is the density at L_\star . The results for each fit are given in Table A.4. The best fit model for the GGs is shown in Fig. 2, where we also compare the radio luminosity function of group galaxies to the total radio luminosity function of radio galaxies in the 3GHz VLA-COSMOS survey, and the radio luminosity function of AGN and the star forming population. We also present the linear fit for BGGs, but exclude the one for SGs for clarity. It is evident that the radio emission due to the star formation over-weighs that from the AGN in lower redshifts, i.e at $z < 1$, except at high radio luminosity bins where the AGN contribution is dominating. This behaviour has been described in Novak et al. (2017); Smolčić et al. (2017b) and agrees with other surveys.

To quantify the contribution of the RLF of group galaxies to the total RLF of the 3 GHz population we divide the power-law of GGs, assuming a fixed slope of $\gamma = -0.75$, with the total RLF from the 3 GHz sample for each redshift bin. This gives the fractional contribution of group galaxies to the total RLF. In the top panel of Fig. 3 we plot the fraction with respect to the radio luminosity at 1.4 GHz up to $10^{25} \text{ W Hz}^{-1}$. The reason for that is the RLF of 3 GHz VLA-COSMOS observations is not well constrained above that luminosity (Novak et al. 2018). Furthermore, we should consider that our model might be a good representation of the universe at $L > 10^{25} \text{ W Hz}^{-1}$, and the COSMOS is not suited for low- z studies due to the small volume coverage at low redshifts. Because of the different total RLF shapes per redshift bin there is a bump in the curve, as expected. The use of a fixed slope of $\gamma = -0.75$ does not impact our calculations as the value is within the errors for the fitted γ values presented in Table A.4.

We also calculate the RLF of all massive galaxies with $M_* > 10^{11.2} M_\odot$, which are 3 GHz sources, and compare it to the total RLF. This fraction is shown in the bottom panel of Figure Fig. 3. We immediately see that X-ray groups contribute even more to radio activity at $z < 1$ than massive galaxies in the field do. We discuss this further in the next section.

4. Evolution of the RLF in galaxy groups

The top panel of Fig. 3 shows that the contribution of GGs to the total RLF increases from $z \sim 2$ to the present day, and in particular for objects above radio luminosities at $10^{23} \text{ W Hz}^{-1}$. This picture suggests an evolutionary scenario for the RLF of galaxy groups. We investigate this further by plotting in Fig. 4 the RLF of GGs, BGGs, and SGs, and their relative contribution to the total 3 GHz RLF as a function of redshift. We see an evolution in the RLF of group galaxies from $z \sim 2$ to the present day by a factor of 3. This is an interesting trend, which is not observed in the total RLF. As seen by the normalisation value of the total Φ_\star for a fixed radio luminosity at $10^{24} \text{ W Hz}^{-1}$, shown with cyan, galaxies in the 3 GHz sample display a decrease in their RLF with redshift, while the RLF of GGs below $z < 1$ is fairly constant (top panel of Fig. 4). Interestingly, Smolčić et al. (2017c)

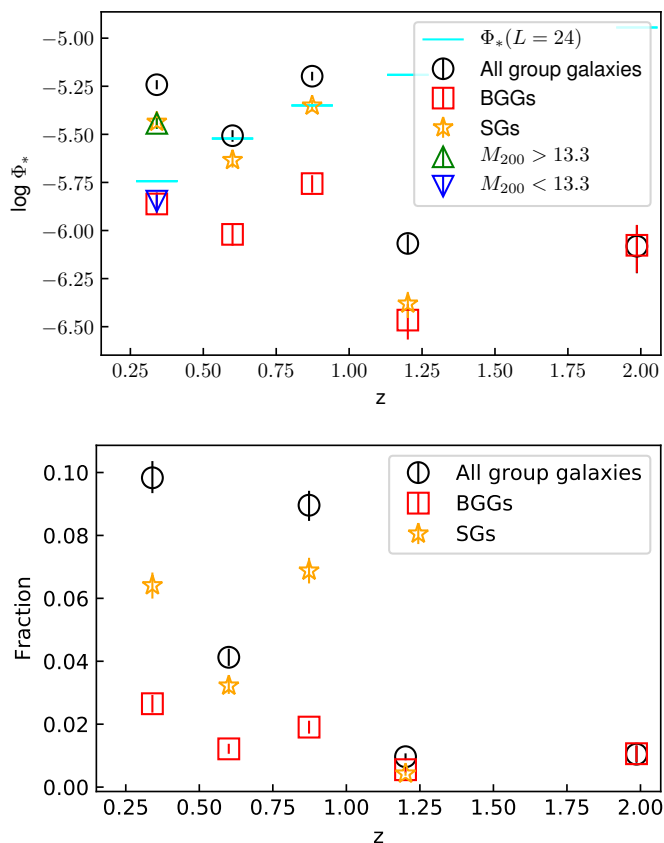


Fig. 4. Top: Radio luminosity function vs redshift for the group galaxies (black circles), brightest group galaxies BGGs (red squares), and satellite galaxies SGs (yellow stars). The low- z redshift bin is split in high ($\log_{10}(M_{200c}/M_{\odot}) > 13.3$) and low ($\log_{10}(M_{200c}/M_{\odot}) < 13.3$) mass halos. Cyan lines show the Φ_* values at $\log_{10}(L_{1.4\text{GHz}}/W \text{ Hz}^{-1}) = 24$ for each redshift bin; these values were placed a dex lower for presentation reasons. Bottom: The relative contribution of GGs to the total radio luminosity, as described in Sec. 3.3, vs redshift. The values plotted here are the ones reported in Table A.4 for $\gamma = -0.75$. Black circles denote GGs, red squares denote BGGs, and yellow stars denote SGs.

show that a similar trend can be reproduced with galaxies. In their Fig. 1 they present a slight increase in the median values of M_* in their radio excess sample above redshift $z = 1$, and a depletion of massive galaxies above $z > 1$, which we also see in the X-ray groups. At the bottom panel of Fig. 3 we see that massive galaxies above $10^{11.2} M_{\odot}$ contribute a large fraction to the total 3 GHz RLF below $z < 1$, contrary to the decreasing RLF in the field. This suggests two things: 1) not all massive galaxies are in groups, but those who remain radio active (Fig. 3); and 2) the increase in the group contribution is because radio activity in groups is nearly constant at $z < 1$, while it is declining in the field (Fig. 4–Top).

The RLF of SGs dominates the RLF of group galaxies up to redshift of $z_{\text{med}} \sim 1.2$, with an overdensity just below $z = 1$ (Fig. 4–Bottom). Scoville et al. (2013) studied the large-scale structure (LSS) in COSMOS and also report a statistically significant overdensity at $z = 0.93$. Above $z \sim 2$ we don’t have a large-enough number of SGs to perform a robust analysis. This is linked to the resolution and sensitivity of the Chandra observations, which results in detecting a small number of group galaxies and satellites in the groups above $z \sim 1.6$ (Fig. 1). The SGs contribute up to $\sim 80\%$ more than the BGGs to the GG RLF below $z_{\text{med}} \sim 1$, as is shown on the bottom panel of Fig. 4. This

highlights how important the identification of SGs within galaxy groups is, and the need for high resolution and sensitivity observations.

The relative contributions of the SGs to the RLF of group galaxies is higher by a factor of 3 than that of BGGs up to $z \sim 1$. Additionally, BGGs contribute a small amount to the RLF of GGs, as seen by the bottom panel of Fig. 4, despite being the most massive galaxies of the group. This is a very interesting result highlighting the importance of identifying the member group galaxies within a group and the need for high sensitivity and high resolution observations.

Splitting the low redshift bin in Fig. 4 in low and high halo mass objects allows us to further identify the contributions to the RLF of galaxy groups. Those with halo masses above $10^{13.3} M_{\odot}$ contribute more to the RLF of GGs than those below, and this contribution is linked to SGs as we mentioned above. The low halo mass points (Table A.4 & Fig. 2) show a faster turnover as we do not expect to detect many low mass, high luminosity objects.

Yuan et al. (2016), who studied brightest cluster galaxies (BCGs), found that RLFs of 7138 BCGs in the range $0.05 < z < 0.45$ do not show significant evolution with redshift. This no evolution pattern of BCGs agrees with our results for BGGs in COSMOS. At the bottom panel of Fig. 4 we see that the RLF of BGGs fluctuates slightly with redshift but it is the RLF of satellites that drives the redshift evolution.

Novak et al. (2018) discuss possible biases which could affect the calculations. These include the assumed shape of the radio SED to be a power law, and the radio excess criterion to be too conservative and thus excluding low-luminosity AGN from the sample. We refer the reader to their discussion (see their Section 3.4). Given that Novak et al. (2018) were able to reproduce the radio sky brightness with the 3 GHz VLA-COSMOS data, we are confident our results, at least for $L_{1.4 \text{ GHz}} < 10^{25} \text{ W Hz}^{-1} \text{ sr}^{-1}$, are robust. Furthermore, Novak et al. (2018) discuss possible biases that affect the RLF of the high luminosity bin, i.e. bright radio but faint in the near-infrared sources ($K = 24.5 \text{ mag}$). We have constrained our sample to halo masses above $10^{13.3} M_{\odot}$, to perform an unbiased analysis. Incidentally, after the halo-mass cut, the remaining group galaxies in our sample are brighter than $K = 24.5 \text{ mag}$.

5. The AGN and SFG contribution to the GG RLF

The group galaxy population has a mixture of contributions from AGN and SFGs. To explore how much these population contribute to the GG RLF, we cross-correlate the X-ray galaxy group catalogue with the sample of Vardoulaki et al. (2021), which is a value-added catalogue at 3 GHz VLA-COSMOS, which includes 130 FR-type (Fanaroff & Riley 1974) and 1818 jet-less compact radio AGN (COM AGN), as well as 7232 SFGs (see Table 5). Radio AGN in the Smolčić et al. (2017a) sample were selected on the basis of their radio excess, as mentioned above. This criterion, due to the 3σ cut applied, excludes several FR-type radio AGN, which were identified in Vardoulaki et al. (2021) and classified as radio AGN because they exhibit jets/lobes. SFGs are objects which do not display radio excess.

To quantify the contribution of these population separately to the group RLF and to the total RLF we calculate their RLF as described in Sec. 3, using the V/V_{max} method. All AGN and SFGs are in groups with halo masses $M_{200c} > 10^{13.3} M_{\odot}$. For the purposes of this analysis, we use the 1.4 GHz luminosities (Schinnerer et al. 2010). The results for the AGN and SFG populations inside galaxy groups are shown in Fig. 5, where we also

Table 1. The AGN and SFGs inside X-ray galaxy groups. Data from (Vardoulaki et al. 2021), cross-correlated with the X-ray galaxy group catalogue (Gozali et al. 2019).

Number of sources	AGN	SFGs
total 3 GHz VLA-COSMOS	1948	7232
same area & z as X-ray groups	1038	6452
X-ray group members	131	242
BGGs	66	40
SGs	65	202

plot the RLF of AGN and SFGs from the sample of Novak et al. (2018) as in Fig. 2 and the total RLF at 3 GHz. In order to compare the RLF of AGN and SFGs which are GGs and total RLF, we follow the analysis in Sec. 3.3. We fit a linear regression and normalise it to $10^{24} \text{ W Hz}^{-1}$ by applying Eq. 8 for $\gamma = -0.75$. The results are shown in Fig. 5.

We further calculate and plot the fractional contribution of AGN and SFGs which lie inside groups to the total RLF at 3 GHz (Fig. 6), by replicating Fig. 3. The fraction was calculated by dividing the RLF of AGN and of SFGs inside galaxy groups to the total 3 GHz RLF. The fractions per redshift bin are curved lines due to the total RLF being curved. We find that there is a significant contribution from group AGN and SFGs at redshifts $z < 1$, and very little contribution above. We present the values for these fractions in Table 2.

Additionally, we explore the fractional contribution of the AGN and SFGs inside GGs to the RLF of GGs, shown in Fig. 6 as dashed-dotted lines. The fraction was calculated by dividing the RLF of AGN and SFGs inside galaxy groups to the GG RLF. We get a constant value across all luminosities in Fig. 6 because the divided fits are both linear. The contribution of AGN RLF to the GG RLF is significant at the redshift bin $z_{\text{med}} = 0.6$ of around 45% and at $z_{\text{med}} = 0.8$ with fraction around 30%. The fraction in SFGs is around 20% for $z_{\text{med}} = 0.6$ and $z_{\text{med}} = 0.8$, while at $z_{\text{med}} = 0.3$ it dominates the GG RLF. The excess we see in the fraction of SFGs at $z_{\text{med}} = 0.3$ can be explained by the linear fit being normalised to $10^{24} \text{ W Hz}^{-1}$ and forced to have a slope of $\gamma = -0.75$. For $z > 1$ the contribution of AGN and SFGs to the GG RLF drops sharply and below 10%. These findings suggest AGN inside groups significantly contribute to the RLF at redshifts between $0.4 < z < 1.0$, and SFGs contribute significantly at $0.07 < z < 0.4$.

There are 66 AGN associated with BBGs and 65 with SGs, as shown in Table 5. For SFGs we get 40 BGGs and 202 SGs. Due to the small numbers of sources per bin, we cannot replicate Fig. 4 by splitting the AGN and SFGs RLF inside groups in BGGs and SGs and calculating their RLF. Fig. 4 suggests the evolution of the GG RLF is driven by satellites. Based on our results on from Fig. 6, at the $z_{\text{med}} = 0.3$ redshift bin, the SG SFGs are responsible for the peak of the GG RLF, while at $z_{\text{med}} = 0.8$ the increase is mainly driven by AGN.

How much of the AGN contribution to the GG RLF comes from extended radio emission, given the capabilities of the 3 GHz VLA-COSMOS survey, is not easy to estimate due to sample size limitations. From Table 5 we see that $\sim 82\%$ of AGN inside galaxy groups are jet-less AGN. But in order to robustly answer this question we need to separate FRs and COM AGN in-

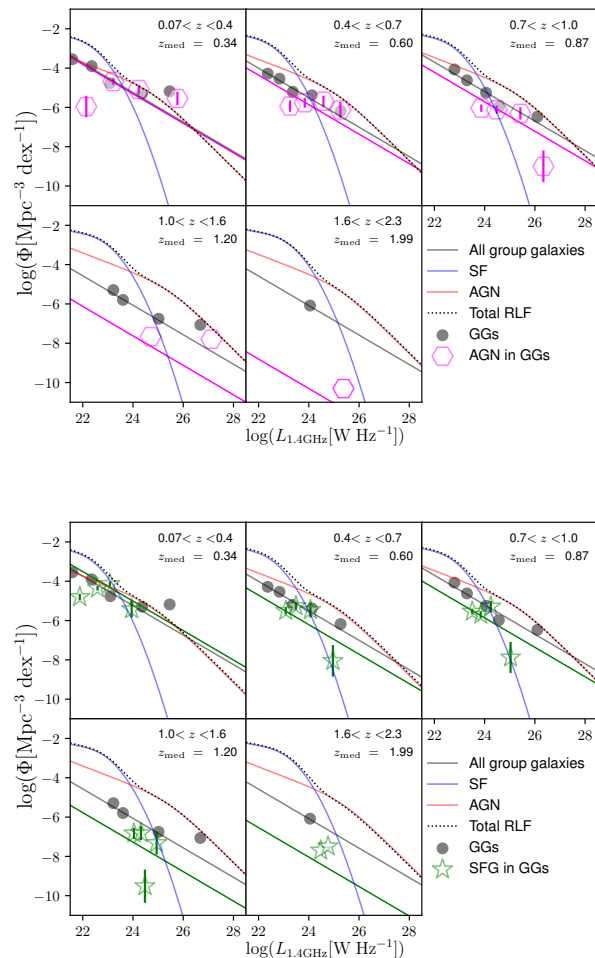


Fig. 5. Total radio luminosity functions of galaxies in groups, as in Fig. 2, including RLFs for different populations: radio AGN inside galaxy groups as magenta hexagons (top) and SFGs inside galaxy groups as green stars (bottom). To compare to the GG sample, we normalise the fit to the AGN and SFGs inside groups to $L_{1.4\text{GHz}} = 10^{24} \text{ W Hz}^{-1}$ and slope of $\gamma = -0.75$. For comparison we show the GG sample (black circles for data, and black solid line with a slope $\gamma = -0.75$ for the fit). The red solid line shows the RLF for all AGN, the blue solid line for all SFGs, and the dotted black line is the total RLF.

side groups and calculate their RLFs per redshift bin, as above, which we cannot do given the small number of FRs per redshift bin. To get an idea of how extended the FRs within the AGN sample are, we have a look at the linear projected sizes D of FRs in Vardoulaki et al. (2021). The sensitivity and resolution of the 3 GHz VLA-COSMOS survey are $2.3 \mu\text{Jy/beam}$ and $0''.75$, respectively. This means that we are able to resolve and disentangle structures of $\sim 6 \text{ kpc}$ at $z \sim 2$. The smallest FR reported in Vardoulaki et al. (2021) has $D = 8.1 \text{ kpc}$ at $z = 2.467$, just above the resolution limit, and the smallest edge-brightened FR has $D = 24.3 \text{ kpc}$ at $z = 1.128$, where the lobes are separated by 8 kpc . Inside X-ray galaxy groups, the smallest FR has $D = 13.37 \text{ kpc}$ at $z = 0.38$ with the most extended having $D = 608.4 \text{ kpc}$ and $z = 1.168$; this is also the most extended object in the Vardoulaki et al. (2021) FR sample. Future surveys with increased sensitivity and resolution will be able to resolve jets and lobes in AGN which appear compact at 3 GHz VLA-COSMOS. With future

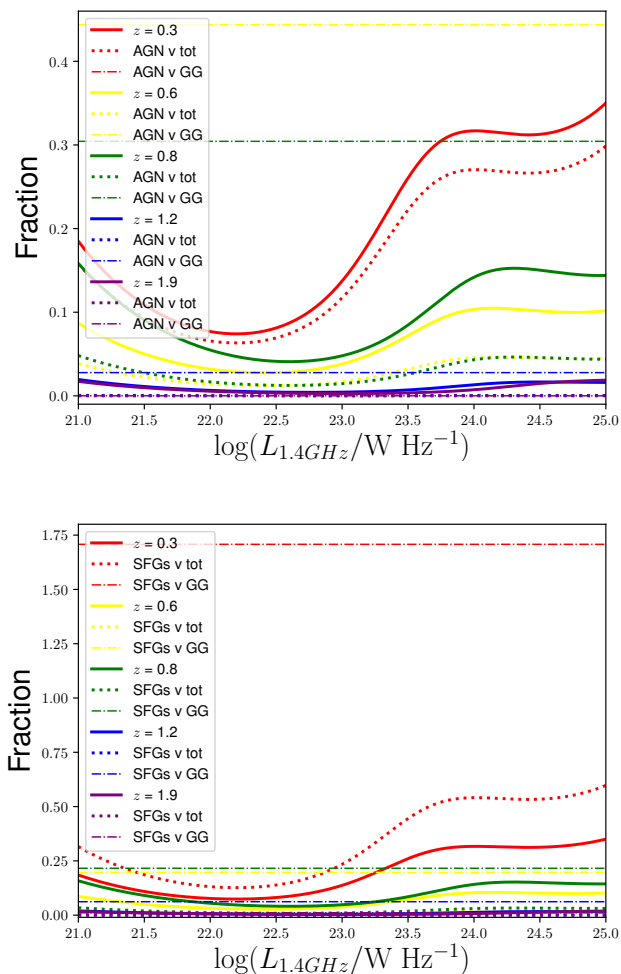


Fig. 6. Fractional contribution to the total radio luminosity function at different epochs vs radio luminosity at 1.4 GHz for GGs (solid lines as in Fig. 3), and for different populations (dotted lines): AGN (top; labelled AGN v tot) and SFGs (bottom; labelled SFG v tot). Dotted-dashed lines show the fractional contribution of AGN (labelled AGN v GG) and SFG (labelled SFG v GG) to the GG RLF. Different colours represent different redshift bins as in Fig. 3

observations at larger sky area and improved statistics we will be in a better position to answer this question.

6. Summary and Conclusions

We presented a study of radio luminosity functions RLFs of group galaxies in the COSMOS field, based on data from the VLA-COSMOS 3 GHz Large Project (Smolčić et al. 2017b) and the X-ray galaxy groups catalogue (Gozali et al. 2019). The X-ray galaxy groups cover halo masses in the range $M_{200c} = 8 \times 10^{12} - 3 \times 10^{14} M_{\odot}$ and the redshift range $0.07 < z < 2.3$. To probe the same group population at all redshifts, we apply a halo-mass cut and only select groups with halo masses $M_{200c} > 10^{13.3} M_{\odot}$. Furthermore, we applied completeness corrections to the calculation of the RLF (Novak et al. 2017) and all galaxy-group members are brighter than $K = 24.5$ mag, which allows for an unbiased analysis.

We calculated the RLF of group galaxies based on the V/V_{max} method and compared it to the 3 GHz RLF from Novak et al. (2018) who fitted the total RLF with pure luminosity

evolution models that depend on redshift. The AGN and SFG populations, characterised by the radio excess parameter, were fitted with a Markov chain Monte Carlo algorithm. We fitted the group galaxies' RLFs with linear and power-law model and estimate their contribution to the total RLF. We also studied how much satellites, brightest group galaxies, AGN, and SFGs contribute to the RLF of galaxy groups and to the total 3 GHz RLF.

Our main results are summarised below:

1. The relative contribution of the group galaxies to the total 3 GHz radio luminosity function in galaxies in the COSMOS field generally decreases with increasing redshift, from 10% locally, to 1% at $z > 1$, with an overdensity just below $z < 1$, in line with large-scale structure studies of the COSMOS field.
2. We see an evolution in the RLF of GGs from $z \sim 2$ to the present day by a factor of 3, which is driven mainly by satellite GGs.
3. The RLF of SGs dominates the RLF of group galaxies up to redshift of $z \sim 1.2$, where we observe a drop in the RLF of both BGGs and SGs almost by a factor of 10.
4. At $z_{\text{med}} = 0.3$, galaxies with halo masses above $10^{13.3} M_{\odot}$ contribute more to the RLF of GGs than those below, and this contribution is linked to SGs.
5. The SG SFGs are responsible for the peak of the GG RLF at $z_{\text{med}} = 0.3$, while at $z_{\text{med}} = 0.8$ the increase is mainly driven by AGN.
6. The increase in the group contribution is because radio activity in groups is nearly constant at $z < 1$, while it is declining in the field. This is not because massive galaxies all get to be in groups, it is because only those in groups remain active.

We showed there is a switch in radio activity at $z = 1$ observed in group environment. It is the galaxies inside groups which remain radio active, compared to the ones in the field. This trend can be reproduced with galaxies as shown by Smolčić et al. (2009, 2017c). Despite the quirk of the COSMOS field with the known overdensity at $z = 0.9$, we used a halo-mass selected sample up to $z = 2.3$ and observed the redshift evolution of the RLF of group galaxies, mainly driven by their satellites. Our a study provides an observational probe for the accuracy of the numerical predictions of the radio emission in galaxies in a group environment.

Acknowledgements. We would like to thank Aritra Basu for useful discussions. EV acknowledges support by the Carl Zeiss Stiftung with the project code KO-DAR.

References

- Barr, J. M., Bremer, M. N., Baker, J. C., & Lehnert, M. D. 2003, MNRAS, 346, 229
- Best, P., Lehnert, M., Röttgering, H., & Miley, G. 2002, in Astronomical Society of the Pacific Conference Series, Vol. 268, Tracing Cosmic Evolution with Galaxy Clusters, ed. S. Borgani, M. Mezzetti, & R. Valdarini, 19
- Best, P. N., Kauffmann, G., Heckman, T. M., & Ivezić, Ž. 2005, MNRAS, 362, 9
- Branchesi, M., Gioia, I. M., Fanti, C., Fanti, R., & Perley, R. 2006, A&A, 446, 97
- Byrd, G. & Valtonen, M. 1990, ApJ, 350, 89
- Civano, F., Marchesi, S., Comastri, A., et al. 2016, ApJ, 819, 62
- Clemens, M. S., Vega, O., Bressan, A., et al. 2008, A&A, 477, 95
- Condon, J. J. 1984, ApJ, 287, 461
- Condon, J. J. 1992, ARA&A, 30, 575
- Condon, J. J., Cotton, W. D., & Broderick, J. J. 2002, AJ, 124, 675
- Delvecchio, I., Smolčić, V., Zamorani, G., et al. 2017, A&A, 602, A3
- Dressler, A. 1980, ApJ, 236, 351
- Elvis, M., Civano, F., Vignali, C., et al. 2009, ApJS, 184, 158
- Fanaroff, B. L. & Riley, J. M. 1974, MNRAS, 167, 31P

Table 2. Fractional contribution f of AGN and SFGs RLFs, inside groups, to the GG RLF and to the total RLF at $L_{1.4\text{ GHz}} = 10^{23}$ and $L_{1.4\text{ GHz}} = 10^{25}$ W Hz $^{-1}$, as in Fig. 6.

z_{med}	$f_{\text{AGN-GG}}$	$f_{\text{AGN-tot23}}$	$f_{\text{AGN-tot25}}$	$f_{\text{SFG-GG}}$	$f_{\text{SFG-tot23}}$	$f_{\text{SFG-tot25}}$
0.3	0.85	0.11	0.29	1.70	0.23	0.59
0.6	0.44	0.01	0.04	0.19	0.007	0.02
0.8	0.30	0.01	0.04	0.21	0.01	0.03
1.2	0.02	1×10^{-4}	4×10^{-4}	0.06	2×10^{-4}	9×10^{-4}
1.9	6×10^{-6}	1×10^{-7}	1×10^{-6}	0.01	3×10^{-5}	2×10^{-4}

Foreman-Mackey, D., Hogg, D. W., Lang, D., & Goodman, J. 2013, PASP, 125, 306

Gozaliasl, G., Finoguenov, A., Tanaka, M., et al. 2019, MNRAS, 483, 3545

Gruppioni, C., Pozzi, F., Rodighiero, G., et al. 2013, MNRAS, 432, 23

Khosroshahi, H. G., Raouf, M., Miraghaei, H., et al. 2017, ApJ, 842, 81

Laigle, C., McCracken, H. J., Ilbert, O., et al. 2016, ApJS, 224, 24

Larson, R. B. 1980, Philosophical Transactions of the Royal Society of London Series A, 296, 299

Magorrian, J., Tremaine, S., Richstone, D., et al. 1998, AJ, 115, 2285

Mauch, T. & Sadler, E. M. 2007, MNRAS, 375, 931

Miller, N. A. & Owen, F. N. 2003, AJ, 125, 2427

Novak, M., Smolčić, V., Delhaize, J., et al. 2017, A&A, 602, A5

Novak, M., Smolčić, V., Schinnerer, E., et al. 2018, A&A, 614, A47

Oemler, Augustus, J. 1974, ApJ, 194, 1

Raouf, M., Khosroshahi, H. G., Mamon, G. A., et al. 2018, ApJ, 863, 40

Reddy, N. A. & Yun, M. S. 2004, ApJ, 600, 695

Sadler, E. M., Jackson, C. A., Cannon, R. D., et al. 2002, MNRAS, 329, 227

Sadler, E. M., Jenkins, C. R., & Kotanyi, C. G. 1989, MNRAS, 240, 591

Schinnerer, E., Sargent, M. T., Bondi, M., et al. 2010, ApJS, 188, 384

Schmidt, M. 1968, ApJ, 151, 393

Scoville, N., Arnouts, S., Aussel, H., et al. 2013, ApJS, 206, 3

Scoville, N., Aussel, H., Brusa, M., et al. 2007, ApJS, 172, 1

Smolčić, V., Delvecchio, I., Zamorani, G., et al. 2017a, A&A, 602, A2

Smolčić, V., Novak, M., Bondi, M., et al. 2017b, A&A, 602, A1

Smolčić, V., Novak, M., Delvecchio, I., et al. 2017c, A&A, 602, A6

Smolčić, V., Zamorani, G., Schinnerer, E., et al. 2009, ApJ, 696, 24

Tabatabaei, F. S., Schinnerer, E., Krause, M., et al. 2017, ApJ, 836, 185

Vardoulaki, E., Jiménez Andrade, E. F., Delvecchio, I., et al. 2021, A&A, 648, A102

Yuan, Z. S., Han, J. L., & Wen, Z. L. 2016, MNRAS, 460, 3669

Appendix A: Numerical results from the calculation of the radio luminosity function in X-ray galaxy groups in COSMOS

Table A.1. Luminosity functions of group galaxies obtained with the V_{\max} method.

z	z_{med}	$\log L_{1.4 \text{ GHz}}$ [W Hz $^{-1}$]	$\log L_{1.4 \text{ GHz}}(\text{med})$ [W Hz $^{-1}$]	$\log \Phi$ [Mpc $^{-3}$ dex $^{-1}$]	N
0.07 – 0.4	0.340	20.787 – 22.000	21.582	$-3.548^{+4.014}_{-4.014}$	28
		22.000 – 22.891	22.355	$-3.900^{+4.811}_{-4.811}$	67
		22.891 – 23.781	23.098	$-4.760^{+5.129}_{-5.267}$	10
		23.781 – 24.671	24.361	$-5.294^{+5.306}_{-5.558}$	3
		24.671 – 25.587	25.459	$-5.181^{+5.283}_{-5.502}$	4
0.4 – 0.7	0.200	22.082 – 22.560	22.364	$-4.284^{+4.710}_{-4.710}$	12
		22.560 – 23.237	22.832	$-4.538^{+5.306}_{-5.306}$	35
		23.237 – 23.913	23.361	$-5.204^{+5.544}_{-5.689}$	9
		23.913 – 24.590	24.125	$-5.384^{+5.608}_{-5.786}$	6
		24.590 – 25.292	25.267	$-6.178^{+5.816}_{-6.26}$	1
0.7 – 1.0	0.073	22.605 – 22.92	22.797	$-4.069^{+4.702}_{-4.702}$	26
		22.920 – 23.715	23.296	$-4.620^{+5.497}_{-5.497}$	58
		23.715 – 24.510	24.056	$-5.254^{+5.856}_{-5.856}$	16
		24.510 – 25.304	24.566	$-5.983^{+5.995}_{-6.248}$	3
		25.304 – 26.125	26.099	$-6.475^{+6.113}_{-6.557}$	1
1.0 – 1.6	0.001	23.083 – 23.391	23.219	$-5.293^{+5.463}_{-5.658}$	5
		23.391 – 24.487	23.601	$-5.794^{+6.377}_{-6.377}$	15
		24.487 – 25.584	25.019	$-6.753^{+6.633}_{-6.943}$	2
		25.584 – 26.707	26.680	$-7.064^{+6.702}_{-7.146}$	1
1.6 – 2.3	0.387	23.746 – 24.159	24.049	$-6.082^{+6.183}_{-6.402}$	4

Table A.2. Luminosity functions of BGGs obtained with the V_{\max} method.

z	z_{med}	$\log L_{1.4 \text{ GHz}}$ [W Hz $^{-1}$]	$\log L_{1.4 \text{ GHz}}(\text{med})$ [W Hz $^{-1}$]	$\log \Phi$ [Mpc $^{-3}$ dex $^{-1}$]	N
0.07 – 0.4	0.344	21.279 – 22.0	21.492	$-4.227^{+4.397}_{-4.591}$	5
		22.000 – 22.889	22.545	$-4.494^{+5.121}_{-5.121}$	18
		22.889 – 23.779	23.138	$-5.148^{+5.25}_{-5.468}$	4
		23.779 – 24.668	24.361	$-5.771^{+5.409}_{-5.853}$	1
		24.668 – 25.583	25.557	$-5.783^{+5.421}_{-5.865}$	1
0.4 – 0.7	0.6	22.202 – 22.56	22.245	$-4.824^{+4.704}_{-5.014}$	2
		22.560 – 23.237	22.930	$-5.114^{+5.483}_{-5.621}$	10
		23.237 – 23.913	23.368	$-5.68^{+5.692}_{-5.944}$	3
		23.913 – 24.590	24.028	$-5.685^{+5.697}_{-5.949}$	3
		24.59 – 25.292	25.267	$-6.178^{+5.816}_{-6.26}$	1
0.7 – 1.0	0.886	22.656 – 22.92	22.761	$-4.911^{+4.923}_{-5.175}$	3
		22.920 – 23.715	23.332	$-5.245^{+5.832}_{-5.832}$	15
		23.715 – 24.510	24.095	$-5.506^{+5.846}_{-5.992}$	9
		24.510 – 25.304	24.566	$-6.461^{+6.099}_{-6.543}$	1
		25.304 – 26.125	26.099	$-6.475^{+6.113}_{-6.557}$	1
1.0 – 1.6	1.161	23.083 – 23.391	23.152	$-5.551^{+5.431}_{-5.741}$	2
		23.391 – 23.959	23.588	$-5.917^{+6.14}_{-6.318}$	6
		23.959 – 24.527	23.978	$-6.733^{+6.372}_{-6.816}$	1
		24.527 – 25.120	25.095	$-6.787^{+6.426}_{-6.87}$	1
1.6 – 2.3	1.987	23.746 – 24.159	24.049	$-6.082^{+6.183}_{-6.402}$	4

Table A.3. Luminosity functions of satellites obtained with the V_{\max} method.

z	z_{med}	$\log L_{1.4 \text{ GHz}}$ [W Hz $^{-1}$]	$\log L_{1.4 \text{ GHz}}(\text{med})$ [W Hz $^{-1}$]	$\log \Phi$ [Mpc $^{-3}$ dex $^{-1}$]	N
0.07 – 0.4	0.34	20.787 – 22.000	21.641	$-3.606^{+4.022}_{-4.022}$	23
		22.000 – 22.891	22.278	$-4.028^{+4.87}_{-4.87}$	49
		22.891 – 23.781	23.045	$-4.987^{+5.211}_{-5.389}$	6
		23.781 – 24.671	24.290	$-5.47^{+5.35}_{-5.66}$	2
		24.671 – 25.587	25.360	$-5.306^{+5.318}_{-5.57}$	3
0.4 – 0.7	0.603	22.082 – 22.560	22.442	$-4.389^{+4.759}_{-4.897}$	10
		22.560 – 22.956	22.727	$-4.544^{+5.181}_{-5.181}$	19
		22.956 – 23.351	23.113	$-4.943^{+5.283}_{-5.428}$	9
		23.351 – 23.747	23.370	$-5.449^{+5.461}_{-5.713}$	3
		23.747 – 24.167	24.143	$-5.478^{+5.49}_{-5.742}$	3
0.7 – 1.0	0.848	22.605 – 22.920	22.798	$-4.125^{+4.727}_{-4.727}$	23
		22.920 – 23.480	23.204	$-4.624^{+5.414}_{-5.414}$	39
		23.480 – 24.040	23.720	$-5.378^{+5.684}_{-5.838}$	8
		24.040 – 24.600	24.391	$-5.707^{+5.809}_{-6.027}$	4
		24.600 – 25.185	25.16	$-6.327^{+5.966}_{-6.41}$	1
1.0 – 1.6	1.23	23.196 – 23.391	23.266	$-5.443^{+5.455}_{-5.707}$	3
		23.391 – 24.487	23.521	$-6.054^{+6.36}_{-6.515}$	8
		24.487 – 25.584	24.943	$-7.054^{+6.692}_{-7.137}$	1
		25.584 – 26.707	26.68	$-7.064^{+6.702}_{-7.146}$	1

Table A.4. Best power law fit parameters.

sample	z	$\log \Phi^*$	γ	$\log \Phi^* (\gamma = 0.75)$
		[Mpc ⁻³ dex ⁻¹]		[Mpc ⁻³ dex ⁻¹]
AGGs	0.07-0.40	-5.281 ^{0.065} _{0.068}	-0.773 ^{0.038} _{0.041}	-5.242 ^{0.024} _{0.024}
AGGs	0.40-0.70	-5.573 ^{0.083} _{0.09}	-0.818 ^{0.08} _{0.08}	-5.507 ^{0.029} _{0.032}
AGGs	0.70-1.0	-5.304 ^{0.039} _{0.043}	-0.997 ^{0.051} _{0.053}	-5.198 ^{0.023} _{0.022}
AGGs	1.0-1.6	-6.09 ^{0.075} _{0.122}	-0.779 ^{0.147} _{0.27}	-6.067 ^{0.047} _{0.051}
AGGs	1.6-2.3	-6.042 ^{0.111} _{0.155}	-1.527 ^{1.034} _{1.01}	-6.082 ^{0.109} _{0.141}
BGGs	0.07-0.40	-5.471 ^{0.082} _{0.088}	-0.542 ^{0.05} _{0.049}	-5.862 ^{0.046} _{0.051}
BGGs	0.40-0.70	-5.851 ^{0.107} _{0.136}	-0.567 ^{0.131} _{0.138}	-6.02 ^{0.053} _{0.059}
BGGs	0.70-1.0	-5.755 ^{0.053} _{0.065}	-0.75 ^{0.075} _{0.077}	-5.756 ^{0.044} _{0.047}
BGGs	1.0-1.6	-6.616 ^{0.117} _{0.156}	-1.318 ^{0.255} _{0.233}	-6.466 ^{0.083} _{0.101}
BGGs	1.6-2.3	-6.046 ^{0.117} _{0.145}	-1.442 ^{1.012} _{1.092}	-6.077 ^{0.106} _{0.143}
SGs	0.07-0.40	-5.752 ^{0.094} _{0.105}	-0.962 ^{0.057} _{0.058}	-5.435 ^{0.03} _{0.029}
SGs	0.40-0.70	-5.923 ^{0.127} _{0.142}	-1.032 ^{0.112} _{0.114}	-5.634 ^{0.036} _{0.039}
SGs	0.70-1.0	-5.637 ^{0.073} _{0.078}	-1.252 ^{0.088} _{0.09}	-5.351 ^{0.029} _{0.03}
SGs	1.0-1.6	-6.982 ^{0.532} _{0.365}	-1.942 ^{1.081} _{0.665}	-6.381 ^{0.062} _{0.074}
High-mass groups	0.07-0.40	-5.173 ^{0.064} _{0.068}	-0.595 ^{0.039} _{0.038}	-5.443 ^{0.027} _{0.029}
Low-mass groups	0.07-0.40	-6.333 ^{0.155} _{0.171}	-1.071 ^{0.087} _{0.088}	-5.847 ^{0.045} _{0.049}

Table A.5. Luminosity functions of AGN inside X-ray galaxy groups obtained with the V_{\max} method.

z	z_{med}	$\log L_{1.4 \text{ GHz}}$ [W Hz $^{-1}$]	$\log L_{1.4 \text{ GHz}}(\text{med})$ [W Hz $^{-1}$]	$\log \Phi$ [Mpc $^{-3}$ dex $^{-1}$]	N
0.07 – 0.4	0.344	21.597 – 22.689	22.141	-5.958 ^{-5.554} _{-6.101}	2
		22.689 – 23.782	23.213	-4.681 ^{-4.591} _{-4.751}	30
		23.782 – 24.874	24.229	-5.090 ^{-4.924} _{-5.170}	10
		24.874 – 25.966	25.769	-5.545 ^{-5.300} _{-5.640}	5
0.4 – 0.7	0.600	22.918 – 23.587	23.255	-5.934 ^{-5.746} _{-6.034}	8
		23.587 – 24.257	23.837	-5.764 ^{-5.606} _{-5.858}	11
		24.257 – 24.926	24.583	-5.686 ^{-5.497} _{-5.785}	8
		24.926 – 25.596	25.258	-6.129 ^{-5.851} _{-6.2482}	4
0.7 – 1.0	0.846	23.493 – 24.204	23.867	-6.039 ^{-5.926} _{-6.114}	20
		24.204 – 24.916	24.483	-6.121 ^{-5.993} _{-6.198}	16
		24.916 – 25.628	25.422	-6.305 ^{-6.083} _{-6.398}	6
		25.628 – 26.340	26.340	-8.998 ^[-8.424] _[-9.227]	1
1.0 – 1.6	1.185	24.393 – 25.886	24.707	-7.662 ^{-7.440} _{-7.852}	6
		25.886 – 27.379	27.123	-7.793 ^{-7.389} _{-8.041}	2
1.6 – 2.3	2.061	24.880 – 25.880	25.380	-10.305 ^{-9.731} _{-11.070}	1

Table A.6. Luminosity functions of SFGs inside X-ray galaxy groups obtained with the V_{\max} method.

z	z_{med}	$\log L_{1.4 \text{ GHz}}$ [W Hz $^{-1}$]	$\log L_{1.4 \text{ GHz}}(\text{med})$ [W Hz $^{-1}$]	$\log \Phi$ [Mpc $^{-3}$ dex $^{-1}$]	N
0.07 – 0.4	0.311	21.246 – 22.049	21.881	-4.799 ^{-4.686} _{-4.850}	20
		22.049 – 22.851	22.589	-4.355 ^{-4.284} _{-4.401}	47
		22.851 – 23.654	23.081	-4.136 ^{-4.050} _{-4.183}	33
		23.654 – 24.456	23.947	-5.427 ^{-5.102} _{-5.521}	3
0.4 – 0.7	0.533	22.692 – 23.258	23.082	-5.502 ^{-5.382} _{-5.577}	18
		23.258 – 23.825	23.487	-5.261 ^{-5.154} _{-5.334}	22
		23.825 – 24.392	24.066	-5.463 ^{-5.185} _{-5.567}	4
		24.392 – 24.959	24.959	-8.052 ^{-7.477} _{-8.279}	1
0.7 – 1.0	0.855	23.277 – 23.716	23.508	-5.543 ^{-5.458} _{-5.604}	34
		23.716 – 24.155	23.842	-5.701 ^{-5.585} _{-5.766}	19
		24.155 – 24.594	24.244	-5.288 ^{-5.085} _{-5.366}	7
		24.594 – 25.033	25.033	-7.879 ^{-7.304} _{-8.096}	1
1.0 – 1.6	1.212	23.792 – 24.116	24.038	-6.828 ^{-6.661} _{-6.947}	10
		24.116 – 24.441	24.318	-6.817 ^{-6.596} _{-6.947}	6
		24.441 – 24.765	24.476	-9.515 ^{-8.941} _{-9.785}	1
		3 24.765 – 25.090	24.941	-7.318 ^{-6.914} _{-7.502}	2
1.6 – 2.3	1.874	24.293 – 24.612	24.472	-7.699 ^{-7.422} _{-7.893}	4
		24.612 – 24.931	24.765	-7.490 ^{-7.245} _{-7.676}	5